Atomically Sharp Crack Tips in Monolayer MoS₂ and Their Enhanced Toughness by Vacancy Defects

Shanshan Wang,[†,§] Zhao Qin,[‡,§] Gang Seob Jung,[‡] Francisco J. Martin-Martinez,[‡] Kristine Zhang,[‡] Markus J. Buehler,*[,‡] and Jamie H. Warner*[,†]

[†]Department of Materials, University of Oxford, Parks Road, Oxford OX1 3PH, United Kingdom

[‡]Department of Civil and Environmental Engineering, Massachusetts Institute of Technology, Cambridge, Massachusetts 02139, United States

Ⓢ *Supporting Information*

ABSTRACT: We combine *in situ* transmission electron microscopy and large-scale molecular dynamics simulations to investigate brittle fracture in 2D monolayer MoS₂, revealing that cracks propagate with a tip of atomic sharpness through the preferential direction with least energy release. We find that sparse vacancy defects cause crack deflections, while increasing defect density shifts the fracture mechanism from brittle to ductile by the migration of vacancies in the strain fields into networks. The fracture toughness of defective MoS₂ is found to exceed that of graphene due to interactions between the atomically sharp crack tips and vacancy clusters during propagation. These results show that monolayer 2D materials are ideal for revealing fundamental aspects of fracture mechanics not previously possible with thicker materials, similar to studies of dislocation behavior in 2D materials.

KEYWORDS: *MoS₂, fracture, crack tips, 2D materials*
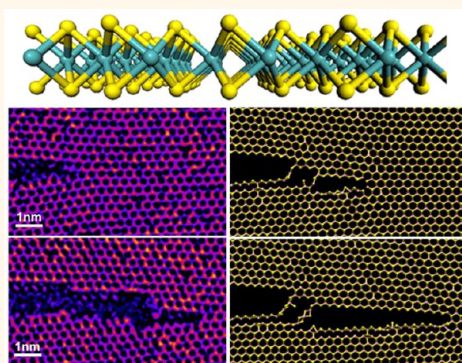
Fracture in a material is centered around the mechanical behavior of cracks and their tips as they develop.[1−9] Brittle fracture is associated with rapid clean cleavage of bonds, and ductile fracture generally involves some plastic deformation around the tip front that slows down the crack propagation.[10] Preventing cracking from brittle propagations can delay mechanical failure and effectively increase the material's fracture toughness. Crack tips with atomic sharpness are predicted to play a major role at the frontier of crack propagation, and therefore, it is important to understand their behavior at the single atom level.[11] However, the non-negligible thickness of samples has been a major factor limiting atomic level *in situ* dynamic studies of crack tip interactions in materials,[12−14] which could be overcome by utilizing ultrathin monolayer 2D materials.

Gaining a deep understanding of fracture mechanics is critical to avoid mechanical failure in materials and requires investigation at the atomic level, due to the nature of bond breakage in crack propagation, the nanoscale size of crack tips, interactions with defects, and the plasticity generated in ductile materials under stress. Among different imaging techniques,[15−18] transmission electron microscopy (TEM) can provide single atom resolution, and the recent rise of 2D materials, such as graphene, MoS₂, and BN, provides material

samples to image the exact atomic structure of crack tips, where the atomic positions can be truly interpreted from their 2D projection.[19,20] Classical molecular dynamics (MD) simulation represents an efficient tool to investigate the mechanics and fracture of different 2D materials. Fracture in graphene has been extensively investigated in simulations with comparison to experiments,[21−25] and there is evidence that defects in graphene do not strongly alter the crack propagation speed.[26] However, it is not clear if all the 2D materials fail in the same way.

Here, we examine the structure and dynamics of cracks in suspended single crystals of monolayer MoS₂ at the atomic level using aberration-corrected TEM (AC-TEM). Cracks were introduced into MoS₂ by popping the strained 2D membrane with a focused electron beam (Figure 1a; see Methods) to cause fractures. MD simulations based on first-principles reactive force fields (see Methods) on the same length scale as experiments are used to reproduce the experimental observations and provide insights into the dynamical behavior.
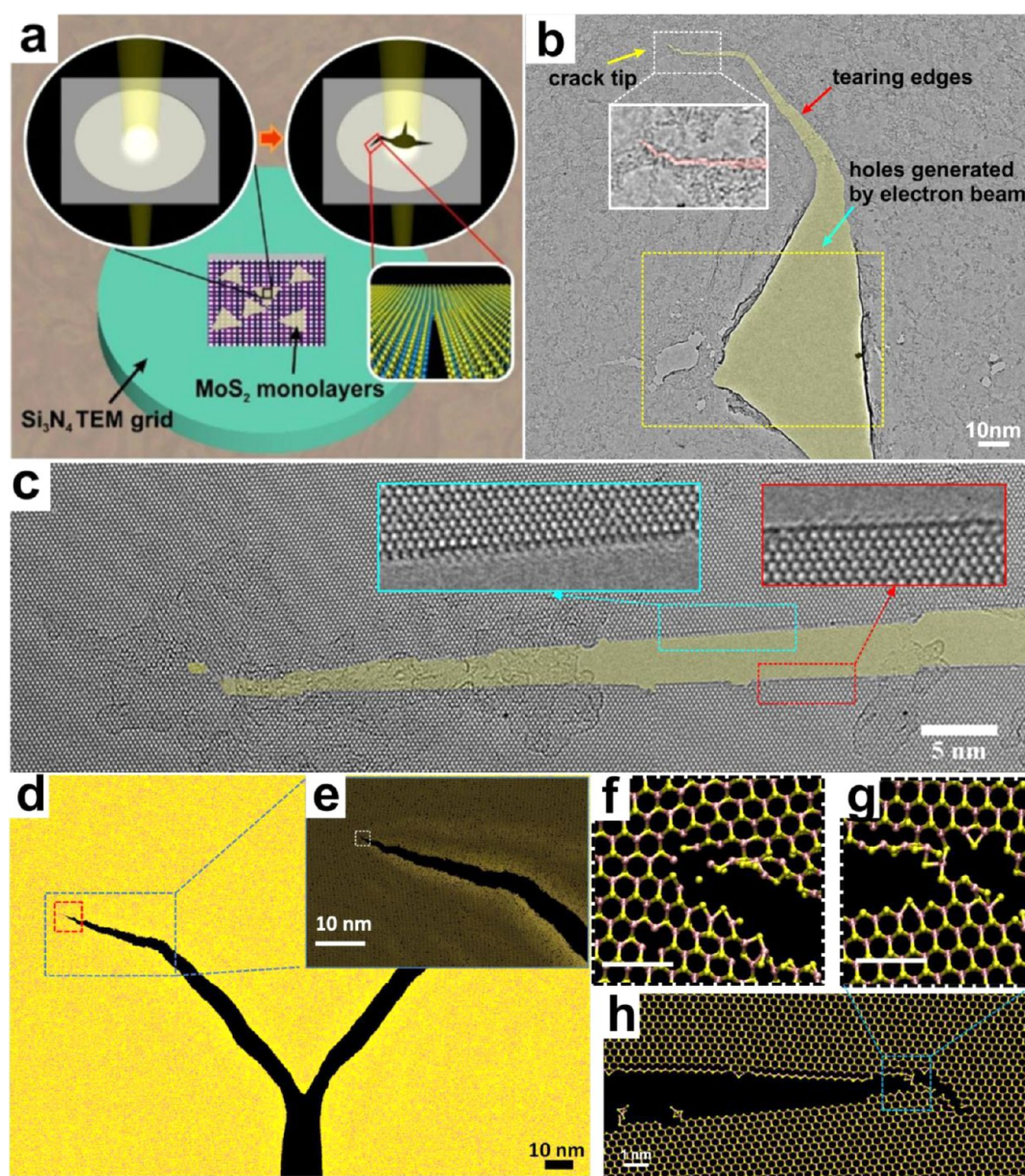
Figure 1. (a) Schematic illustration showing CVD-grown triangular monolayer MoS_2 domains with the size of ∼15 μm transferred onto a Si_3N_4 TEM grid with arrays of 2 μm holes. Each domain can completely cover several holes. The zoomed-in image of the circular window shows the crack generation process by the focused e-beam on the suspended monolayer MoS_2 membrane covering one TEM hole. (b) TEM image showing the crack microstructure. The crack was developed from a hole created by continuous focused e-beam irradiation, marked by the yellow box. A typical crack propagated along a certain lattice direction can be seen (masked by a half-transparent yellow color), leaving long and straight edges, highlighted by the red arrow. The white dashed box shows the crack morphology (highlighted by a half-transparent red color) in its final propagation stage including the crack tip, with a higher-magnification image below as an inset. (c) Montage of AC-TEM images stitched together to show the long-range atomic sharpness of the edges of the crack. The shape of the crack is highlighted in yellow. Insets show magnified AC-TEM image of the edge configurations. (d,e) Snapshots of MD simulation of the crack propagating from the end of an elliptical hole in a piece of the 200 by 200 nm^2 MoS_2 model under mechanical stretching force. The crack tip shows an atomic sharpness feature. (f–h) MD simulation snapshots of a different crack propagated by creating a smooth crack edge before creating a step and breaking bonds in front of an intact Mo−S bond, leaving a residue chain behind the crack tip.

RESULTS AND DISCUSSION

Figure 1b shows a low-magnification TEM image of the region where the electron beam has popped the MoS_2 membrane by sputtering a hole, indicated with the yellow dashed boxed area, and the cracks that emanated into the surrounding area of the MoS_2 that had not been subjected to electron beam irradiation. The region of the crack tip is indicated by the white dashed box, Figure 1b, and the inset shows a magnified view of this area. The cracks were found to have zigzag edge terminations, as shown in Figure 1c, that are long and straight and indicative of brittle fracture along the crystallographic plane. Large-scale MD simulations also predict the presence of cracks propagating from the end of an elliptical hole (Figure 1d,e), along the zigzag direction with similar zigzag edge terminations. Snapshots from the MD simulations reveal that the crack can narrow to an apex tip with atomic sharpness and in some cases have reconstructed tips that contain atomic chains bridging the gap (Figure 1f–h).
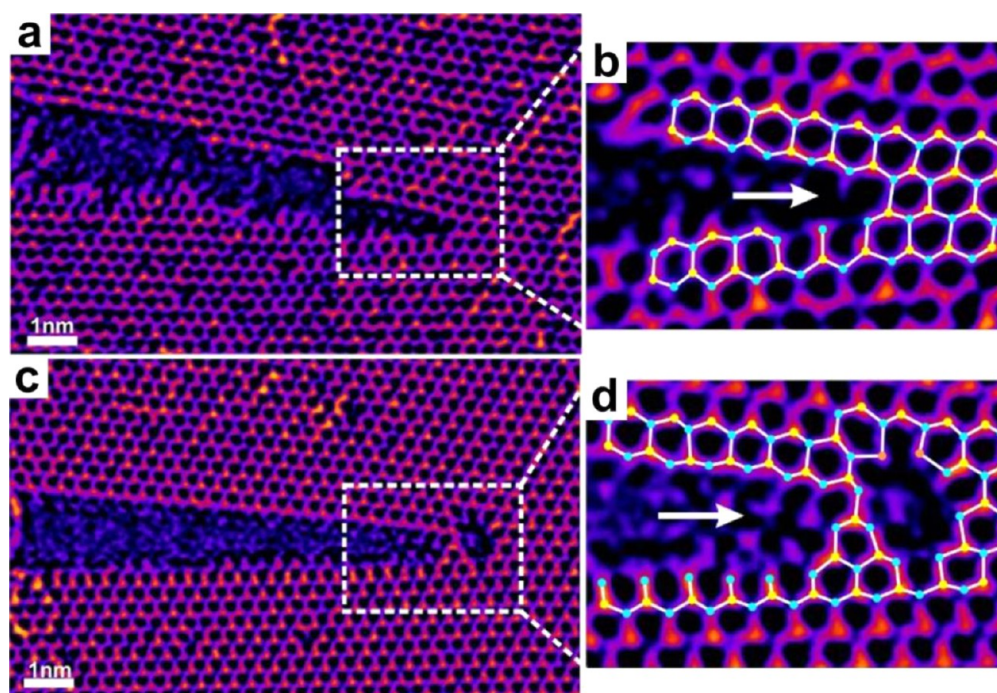
Figure 2. Structure of atomically sharp and reconstructed crack tips. (a) AC-TEM image of an atomically sharp crack tip in MoS$_2$ and (b) magnified image with atomic model overlay. (c) AC-TEM image of a reconstructed sharp tip in MoS$_2$ and (d) magnified image with atomic model overlay.
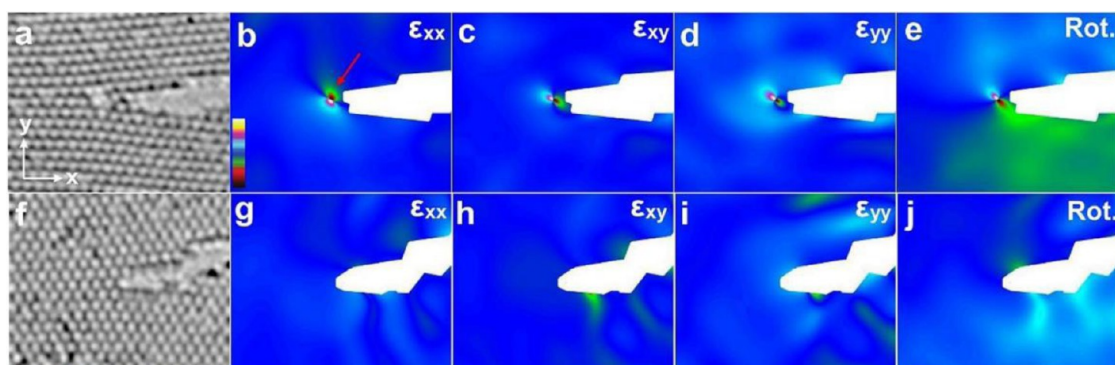

Figure 3. Strain analysis of different crack tips. AC-TEM images of crack tips (a) reconstructed with dislocation and (f) nonreconstructed and dislocation free. (b–e) Strain components, ε_{xx}, ε_{xy}, ε_{yy} and rotation (radians), extracted by GPA from AC-TEM image in (a). Red arrow indicates strain feature associated with the dislocation core. Scale bar in (b) ranges from −1 to +1 and is used for all components except rotation. (g–j) Strain components, ε_{xx}, ε_{xy}, ε_{yy} and rotation (radians), extracted by GPA from AC-TEM image in (f).

Analysis of AC-TEM images for several different crack tips showed excellent agreement with the MD calculations (Figure 1f,g), with the two different types of sharp tips (atomically sharp and reconstructed) observed (Figure 2a–d). The AC-TEM image in Figure 2b shows that the crack narrows all the way down to a single Mo−S bond at its tip, indicated with an arrow. A schematic illustration based on experimental observations, which indicates a possible movement of atoms required to form the reconstructed tip, is supplied in Figure S10.

The differences in the strain fields of the reconstructed tip (Figure 3a) and atomically sharp tip (Figure 3f) were evaluated using geometric phase analysis of the AC-TEM images. This method is effective at identifying dislocations from their strain profile and understanding rotation effects in the lattice. The strain maps from the reconstructed crack tip (Figure 3b–e) show the typical pattern in the ε_{xx} and ε_{yy} strain maps (Figure

3b,d) for a dislocation at the front of the reconstructed region, which is not observed in the atomically sharp crack tip strain maps (Figure 3g,i). The magnitude of the rotation strain appears larger for the reconstructed tip (Figure 3e) compared to the atomically sharp tip (Figure 3j). The use of geometric phase analysis (GPA) in Figure 3 clearly shows the difference between the two types of tip structures.

Crack propagations in MoS$_2$ can be straight for up to 1 μm, forming atomically smooth edges of over nanoscale distances (Figure 4a–d). Very tiny (sub-nanometer) crack deflections are observed across one or two rows of lattice (Figure 4a). Interestingly, unlike graphene, for which cracks occur along both armchair and zigzag lattice directions,[25] in monolayer MoS$_2$, cracks predominantly occur along the zigzag lattice direction. The cracks have complementary atomic edge terminations, indicative of cleaving of the Mo−S bond along the zigzag direction, as shown in Figure 4b−d (Figures S2 and
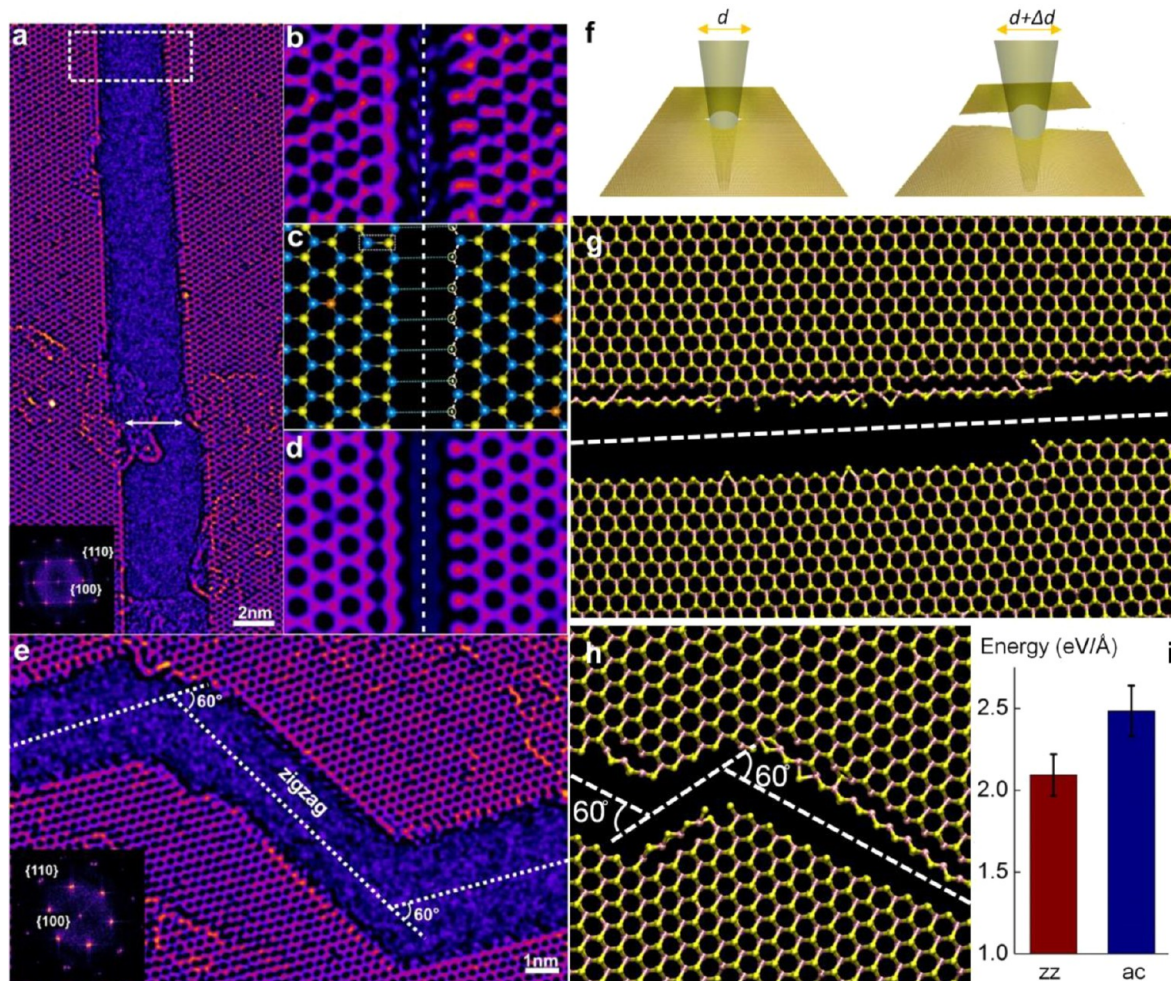
Figure 4. Edge structures of a brittle fracture on MoS_2. (a) AC-TEM image of long and straight zigzag crack edges. The inset is the Fourier transform of the image with labels of two main families of 2D MoS_2 crystal planes, {100} and {110}. (b) Detailed structure of the MoS_2 edges from the region indicated by the white dashed box in (a). (c) Atomic model of the edge structure in (b). The blue, yellow, and orange spheres represent the single Mo atom, double S atoms, and the single S atom, respectively. The yellow circles represent the missing S atoms, and the series of horizontal blue dashed lines are drawn to help show the alignment between these two edges. (d) Multislice image simulation using the atomic model in (c) in a supercell. (e) AC-TEM image showing changes of crack direction along the zigzag lattice direction. The inset is the Fourier transform of the image, confirming the zigzag direction of each edge. (f) Simulation snapshots of the MoS_2 model before and after loading by penetrating with a rigid cylindrical beam as schematically shown. Each model is initially built with a circular hole of 10 nm in diameter and two initial cracks with 30° sharpness and 2 nm length. Increment in the diameter of the beam generates the driving force for the crack to propagate. We test models of different lattice directions (zigzag versus armchair) with respect to the direction of the initial cracks. Snapshots of the crack edges after rupturing along the zigzag (g) and armchair (h) directions. (i) Energy release after crack propagation in two different directions.

S3). Occasional 60° direction changes of the cracks following zigzag orientations are observed (Figure 4e), and the near-perfect unzipping along all directions demonstrates brittle fracture.

MD simulations show that cracks heading in the zigzag direction have smooth propagation with tiny deflections, while a crack heading in the armchair direction propagates with more deflections of 60° (Figure 4g,h). The computed energy release from MD simulations along the zigzag direction is 2.09 ± 0.13 eV/Å, lower than the armchair direction of 2.48 ± 0.16 eV/Å, agreeing with previous density functional theory (DFT) calculations of 2.21 eV/Å for zigzag directions (Figure 4i). Such a difference in energy release explains the predominant zigzag crack propagation direction. The ratio of the energy release is very close to the ratio of the total crack length (cos 30°), suggesting that the increment in the crack path length for

the atomic crack tip mainly contributes to the delayed crack propagation along the armchair direction.

Exposing the crack tip region to the e-beam causes propagation within a fixed location (Figure S4a–c). A fracture speed of ~0.2 nm/s was found under these conditions (Figure 5a–c) and is slow enough to capture the dynamics with atomic resolution in AC-TEM. The e-beam introduces S vacancies into the MoS_2 lattice, causing crack path deflections (Figure 5d–f). The crack structures studied in Figures 1–4 had fast propagation in pristine regions of the MoS_2 that were not exposed to the e-beam and therefore had minimal defect density. Simulations with 1% S vacancies under the same loading condition (Figure 4f) show different crack propagation compared to pristine MoS_2 (Figure 5j–m), in agreement with the experimental results. Deflection occurs at a region between the two S vacancies, and once the crack front passes through, the two S vacancies disappear (Figure 5e) due to vacancy
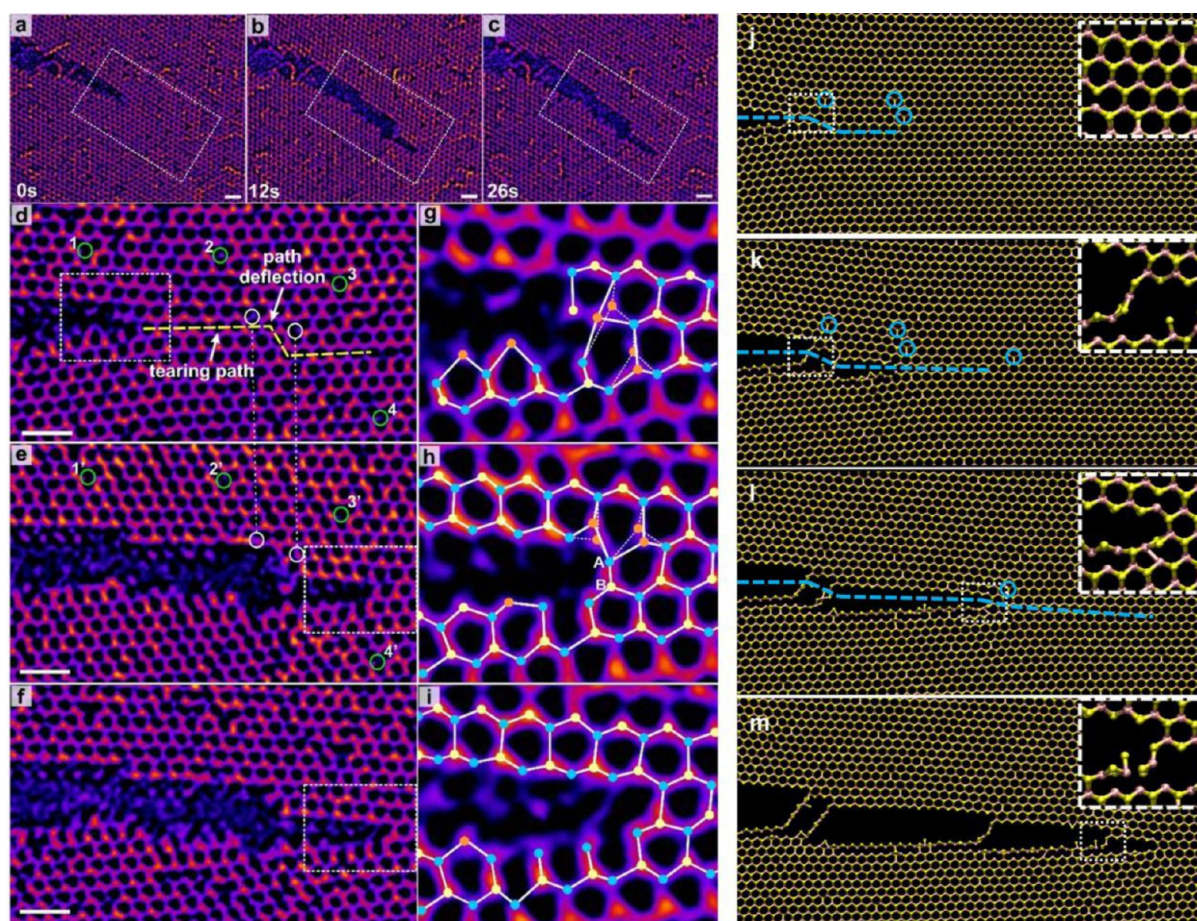
Figure 5. Time series of AC-TEM images showing *in situ* dynamics of MoS$_2$ crack propagation in a mildly defective region. (a−c) Time series of AC-TEM images showing crack movement through a mildly defective region with a low concentration of S vacancies. (d−f) AC-TEM images showing the detailed propagation of the crack tip, marked in the region of the white dashed boxes in (a−c), respectively. The white circles in (d) indicate two S vacancies close to the crack path. However, these two vacancies disappeared after the crack tip passes through, as two locations with sitting S vacancies were replaced by regular double-stacked S atoms, marked by two white circles in (e). The yellow dashed line in (d) represents the tiered path of the crack front, with a white arrow indicating the path deflection point situated between two S vacancies. The green circles numbered from 1 to 4 are used to show four S vacancy defects located farther away from the tiered path, compared to those two vacancies marked by white circles. Their locations in (e) are labeled by green circles with corresponding numbers from 1′ to 4′, respectively. (g−i) AC-TEM images of the crack tip region marked in white boxes in (d−f), respectively, with atomic models overlaid. The blue, yellow, and orange circles represent the single Mo atom, double S atoms, and the single S atom, respectively. All scale bars are 1 nm. (j−m) Simulation snapshots of the crack propagation in a MoS$_2$ model with 1% S atom missing, showing the crack pathway is deflected by the defects near the crack tip.

migration induced by stress concentration around the crack tip. Because of the mobility of vacancies in the stress field, the location of the crack deflection point is not simply determined by the position of static defects, but instead is an evolving dynamic process of vacancy migration and crack propagation by bond unzipping.

In addition, stress concentrated at the crack tip induces lattice distortions, causing the regularly stacked double S atoms in the (001) crystal orientation to split (Figure 5g,h as well as Figure 5j,k) in simulations (Figure S6d−g). However, there is no obvious lattice reconstruction in the tip region. The crack typically propagates by directly unzipping the Mo−S bond (marked by A and B in Figure 5h) perpendicular to the torn path along the zigzag direction. Once the crack tip passes, the distortion in the bonding is reduced, but with some of the S atoms on the S-terminated edge lost or reconstructed to out-of-plane positions.

Increasing the vacancy defect concentration in front of a crack tip results in distinctly different crack propagation

behavior, with some of the single S vacancies agglomerating into line defects followed by the formation of dislocations and microcracks ahead of the tip and small regions of dislocation-free lattice trapped between (Figure 6a−e). Simulations show similar dislocation formation when increasing S vacancy density up to 20% (Figure 6j−n). The Burgers vector of the dislocation region shows two types, (1,0) dislocation and (1,0) + (0,1) dislocation, constructed from two $|b(1,0)| = 3.1$ Å dislocations of (1,0) and (0,1) (Figure 6f−i).[27] All of these dislocation forms can be identified in the simulation snapshots at the crack tip, as shown in Figure 6o−r for moderately defective samples. The continuous creation of dislocations ahead of the crack front decreases the vacancy density in this region (compare Figure 6a with Figure 6d,e), indicating that the dislocations are partially generated by the aggregation of vacancy defects. Furthermore, large-area dislocation pools are formed by the coalescence of small dislocation cores with a dislocation-free microcrack (Figure 6h,i). A fracture velocity of ∼0.07 nm/s in this moderately defective region is the lowest speed measured,
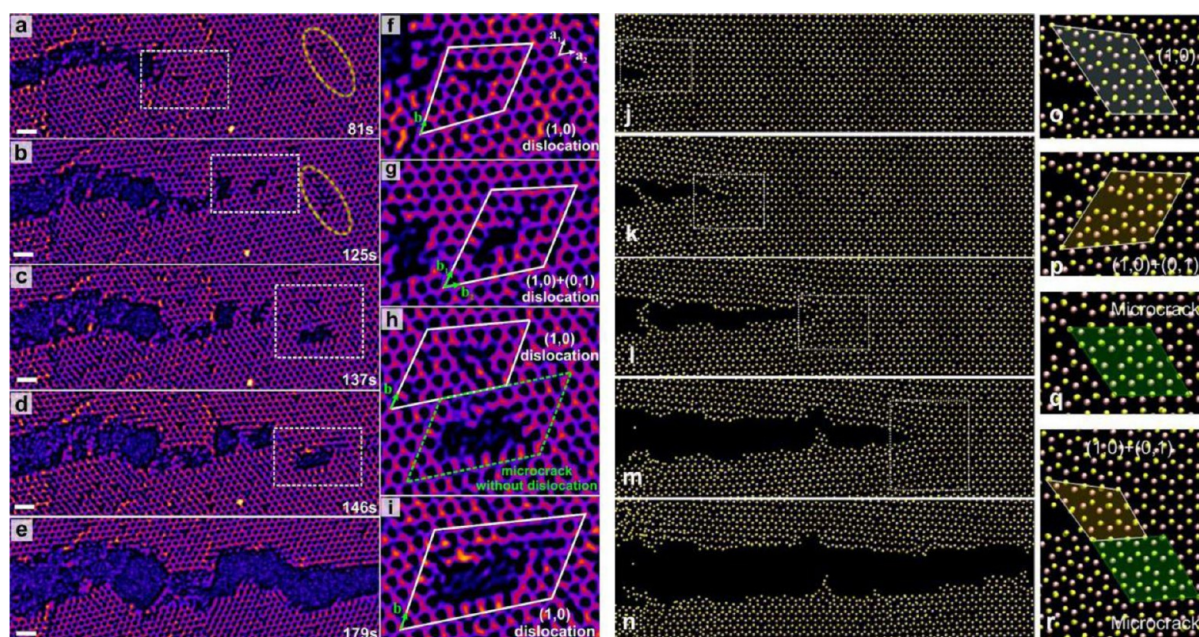
Figure 6. Time series of AC-TEM images showing the *in situ* crack propagation within a moderately defective MoS$_2$ region containing an increased number of vacancy defects. (a–e) Time series of AC-TEM images of crack propagation across an area with a medium concentration of S vacancies, showing the creation of dislocations and microcracks ahead of the crack tip marked by white dashed rectangles. The yellow ellipses in (a,b) show the aggregation of some S vacancies into line defects, which subsequently evolve into dislocation pools in (c) as the crack tip approaches. (f–i) AC-TEM images of regions marked in white dashed boxes in (a–d), respectively. Dislocations with corresponding Burgers vectors, labeled by green arrows, are shown by drawing Burgers circuits in white. Dislocation-free microcrack is marked by green dashed lines. All scale bars are 1 nm. (j–r) Simulation snapshots of the crack propagation in a MoS$_2$ model with 20% S atoms missing, showing various types of dislocations formed at the crack tip. The dislocations interact with the crack propagation by deflecting the crack path and making the crack tip less sharp than material samples with lower defect rates.

compared to the pristine and mildly defective regions (Video 2 and Supporting Information).

Using MD simulations, we find that the defects in MoS$_2$ beyond a critical density can generate a strong collective effect to delay the propagation of an atomic crack tip, and such a mechanism is not shown in graphene. In Figure 7a, we schematically show that randomly distributed S vacancy defects beyond 10% in MoS$_2$ aggregate to form line defects that are distinctly different from the vacancy aggregates in graphene, for which increasing vacancy density results in dislocation pairs and then finally small holes. This result is supported by the observation that the application of e-beam dose to MoS$_2$ in AC-TEM results in vacancies aggregating to form line defects (Figures S5–S8). Our computational simulations of MoS$_2$ (Figure 7b) and graphene (Figure 7c) show that the line defects in MoS$_2$ help to guide and deflect the crack in propagation but the small holes and dislocation in graphene do not affect the crack propagation. This mechanism contributes to the enhanced energy release rate (G_C) and fracture toughness (K_{IC}) for defected MoS$_2$ but not for graphene (Figure 7d,e and Supporting Information Tables 1 and 2). It is noted that our calculations for graphene fracture agree with previous experimental and simulation results.[23,28] Surprisingly, the fracture toughness for mildly and moderately defective MoS$_2$ can exceed that of graphene (Figure 7e). This is attributed to the way in which the atomically sharp crack tips interact with the line defects in MoS$_2$ compared to graphene.

CONCLUSION

In summary, our findings enable validation of many theoretical and computational studies that form the foundation of fracture

mechanics, but which were previously too difficult to observe at the single atom level in thick materials. Crack tips remained atomically sharp during propagation and in dislocation nucleation. The atomically sharp crack does not have infinitely large stress at the tip because the interactions between defects and crack tip can lead to deflections, crack blunting, and plastic yielding by rearranging of the defects. Increasing the density of defects in MoS$_2$ leads to enhanced fracture toughness, which was not observed in graphene, as crack tips become blunt and the propagation speed reduces dramatically, which is associated with increased fracture toughness.

METHODS

Chemical Vapor Deposition Growth of Monolayer MoS$_2$. MoS$_2$ monolayers were grown using a hydrogen-free chemical vapor deposition (CVD) method in atmospheric pressure with precursors of molybdenum trioxide (MoO$_3$, ≥99.5%, Sigma-Aldrich) and sulfur (S, ≥99.5%, Sigma-Aldrich) powder, similar to previously reported strategies with some modifications.[29,30] The MoO$_3$ monolayers were grown on the SiO$_2$/Si (300 nm thick SiO$_2$). To avoid cross-contamination between MoO$_3$ and S powder at high temperatures, the MoO$_3$ precursor was initially loaded in a smaller diameter tube of around 1 cm, which was then placed into the larger 1 in. quartz tube for the entire CVD growth, while the S powder was put in the outer tube. The mouth of the inner tube, which was located near the gas inlet, was positioned upstream more than 15 cm from the position of S, which can thoroughly prevent the S vapor from spreading into the inner-tube and reacting with MoO$_3$. Two furnaces were applied to provide a better temperature control for both precursors and the substrate. S powder and the substrate (with face up) were placed in the central area of the first and second furnace, respectively, while MoO$_3$ powder was loaded at the upstream of the second furnace. The heating temperatures for S, MoO$_3$, and substrate were ~180, ~300, and ~800
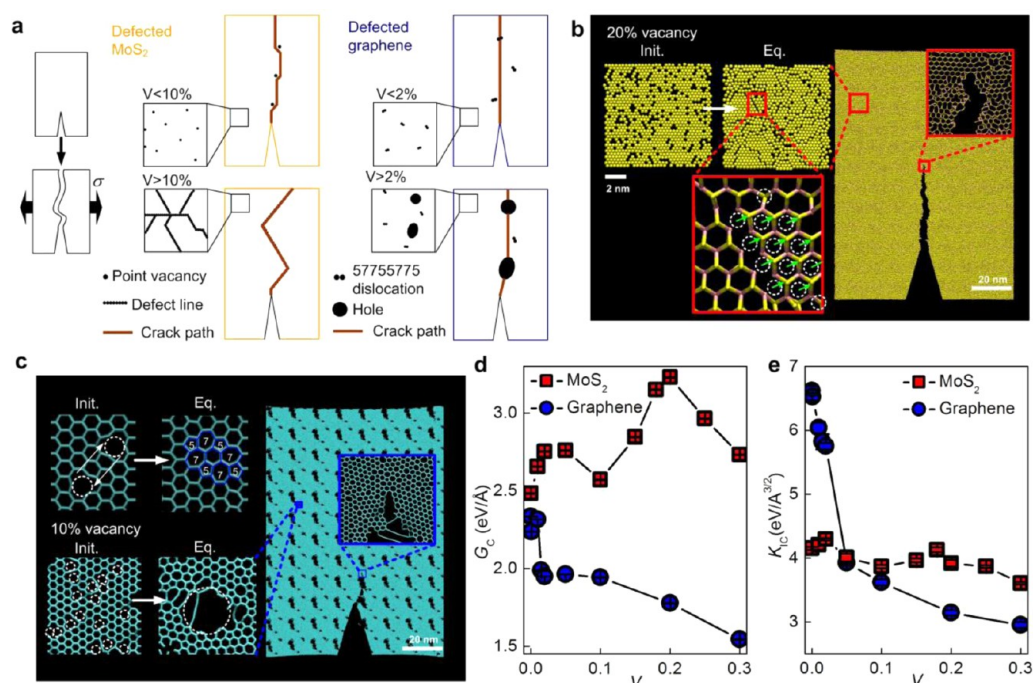
Figure 7. Enhanced fracture toughness of defected MoS_2 and its molecular mechanism. (a) Schematic shows that we apply tensile loading force to material samples on the left and right boundaries until their total failure in our computational simulations. Fracture of defected MoS_2 with different vacancy density (V) is featured by the deflected crack pathway, which is very different from what is seen in graphene. The crack path associates with the conformation of defects at equilibrium as vacancies in MoS_2 can aggregate and form a defect network composed of lines to guide the crack propagation. (b) Simulation snapshots of a defected MoS_2 sample with initially randomly distributed defects with $V =$ 20% before and after equilibration, which shows the merging of vacancies and forming of a defect network. The defect network deflects the crack pathway during fracture. (c) Simulation snapshots of a defected graphene sample with initially randomly distributed defects with $V =$ 10% before and after equilibration, while two neighboring vacancies can be healed by forming a 57755775 dislocation, more vacancies form holes instead. The crack pathway in graphene is not significantly deflected. (d,e) Comparison of the energy release rate (G_C, panel d) as the energy release of unit length of the 2D material during fracture and fracture toughness (K_{IC}, panel e) as a function of vacancy density for MoS_2 and graphene, which shows MoS_2 has a higher energy release rate and a fracture toughness superior to that of graphene once mildly or moderately defected.

°C with argon used as the carrier gas. After a preintroduction of S vapor for ~15 min, the temperature for the second furnace was first increased to ~800 °C at a ramping rate of 40 °C/min and maintained for 15 min under 150 sccm argon flow. Next, the argon flow was reduced to 10 sccm and kept for 25 min before the growth stopped, followed by a fast cooling process. The temperature for S was retained at ~180 °C during the whole synthesis period.

Transfer of MoS_2 Monolayers. To transfer the MoS_2 monolayers onto the TEM grid, a thin film of poly(methyl methacrylate) (PMMA) was spin-coated on the surface of the $MoS_2/SiO_2/Si$ substrate, followed by floating the sample on a 1 mol/L potassium hydroxide solution to etch SiO_2 away. After it was peeled off, the PMMA/MoS_2 film was then transferred into deionized water several times to wash off any residual contamination from the etching process. The rinsed PMMA/MoS_2 film was subsequently scooped up by a holey Si_3N_4 TEM grid (Agar Scientific Y5358), air-dried overnight, and baked at 180 °C for 15 min to ensure a strong interfacial contact between MoS_2 monolayers and the TEM grid. Finally, the PMMA scaffold was removed by submerging the TEM grid in acetone solution for 8 h. To thoroughly remove the hydrocarbon contamination absorbed on the MoS_2 surface, we buried the Si_3N_4 grid in the powder of active carbon with a heating process in the air at 180 °C for 1 h before imaging.

Transmission Electron Microscopy and TEM Data Processing. HRTEM imaging was conducted using Oxford's JEOL JEM-2200MCO field emission gun TEM with a CEOS imaging aberration corrector under an accelerating voltage of 80 kV. AC-TEM images were recorded using a Gatan Ultrascan 4k × 4k CCD camera with 1−2 s acquisition time. We took one frame approximately every 10−20s in our AC-TEM imaging depending on the speed of the crack propagation and the imaging condition adjustment. Images were

processed using ImageJ software. They were initially adjusted with a band-pass filter (between 100 and 1 pixel) to modify the long-range nonuniformity on the illumination intensity and then smoothed by applying a Gaussian blur (2 pixels). The original grayscale images with black atom contrast were inverted, and then a "fire" false color LUT was used to improve the visual contrast. Atomic models were established using Accelrys Discovery Studio Visualizer. Simulated multislice images based on corresponding atomic models were generated using JEMS software with a proper parameter adjustment (defocus spread = 5−6 nm, defocus = 1−2 nm) according to the TEM experimental conditions. We introduced cracks in an intact monolayer MoS_2 by exposing this strained membrane to a focus electron beam under 80 kV, which is similar to prior work.[31] A homogeneous in-plane tension in suspended MoS_2 monolayers was introduced by the baking process during transfer due to the thermal expansion coefficient mismatch between the Si_3N_4 membrane and MoS_2 monolayers. The following *in situ* crack propagation study was also triggered by a proper dose of electron beam irradiation on a MoS_2 area during imaging, causing the crack to move.

Tuning a Reactive Force Field for MoS_2 Modeling. In the present work, we utilize the reactive many-body force field (FF).[32,33] The FF can describe nonlinear behaviors of MoS_2 and simulate breaking and re-forming bonds of materials and deal with the effects of sulfur vacancies. The failure strains of the system under the uniaxial loading depend on the radius cutoff distances among the atoms. We tune the parameters of the original FF based on our DFT calculations because the original FF was not tuned for the failure of MoS_2 system and resulted in artificial stiffening due to the switching function, as with the REBO potential for graphene (see Figure S1 and supplementary discussion 9 in the Supporting Information). To the

best of our knowledge, we first provide the parameters for the stress–strain behaviors comparable with the results from DFT. We obtain the stress–strain curves in the armchair and zigzag directions from DFT calculations by the Quantum-Espresso package[34] using the Perdew–Burke–Ernzerhof functional[35] and norm-conserving-type pseudopotential.[36] The rectangular shape cell contains six atoms with the periodic boundary condition. To model the single-layer MoS_2, a vacuum space of 12 Å in the z direction is inserted to avoid interactions between periodic images. The energy cutoff for the wave functions is 80 Ry, and $10 \times 10 \times 3$ grids are adopted for the k space sampling. The obtained failure engineering strains are 0.36 and 0.26 for the x and y directions, respectively, which shows good agreement with the previous DFT calculations.[37−39] We then prepared the pristine monolayer MoS_2 in 5×5 nm for the tensile tests with molecular dynamics by using the reactive force field. Based on the various combination tests of radius cutoffs, we obtained close failure engineering strains, 0.35 and 0.27 in the x and y directions, respectively. The cutoffs (R_{min}, R_{max}) of Mo−Mo, Mo−S, and S−S are set to (4.5, 5.0), (2.85, 2.85), and (1.1, 2.8) Å, respectively. The radius cutoffs are carefully selected not only to match the failure strains but also to remove artificial stiffening effects caused by the switching function.[40] In another 2D system, graphene, these tuning processes have been widely adopted in both pristine and defected graphene to describe the failure and crack propagations.[23,41] Next, we rescale the repulsion and attraction coefficients of the reactive FF simultaneously (a rescaling factor ∼0.78) to match the stress–strain points under the uniaxial tensile strain of 0.1 in the DFT calculation. By using the strategy, we fine-tune the force field and enable our molecular dynamics simulations to have good agreement with DFT calculation results for the material strength, failure strain, and elastic properties in different material directions. We note that we mainly consider the failure strain and strengths of MoS_2 to tune the parameters because these factors are most critical to describe the failure correctly, which causes an error around 10% of elastic constants from DFT results. The elastic constants and stress–strain curves of the current reactive FF are shown in extended data (Figure S1).

Monolayer MoS_2 Model for Molecular Dynamics Simulations. For the MoS_2 model in a mechanical penetration test in molecular dynamics simulations, we use a 50×50 nm monolayer MoS_2 size with an initial circular hole at the center of the sample. The hole is 10 nm in diameter, and it has two initial triangular cracks at its periphery of two opposite points, as shown in Figure 4f. Each initial crack has 30° sharpness for its crack tip and is 2 nm long. We incorporate the cohesion between the bottom layer of S atom in MoS_2 and the substrate by using a Lennard-Jones (LJ) intermolecular potential with the 9−3 form of[42]

$$E_{S\_Si_3N_4} = \epsilon \left[\frac{2}{15} \left(\frac{\sigma}{r} \right)^9 - \left(\frac{\sigma}{r} \right)^3 \right] \tag{1}$$

where r is the distance from a S atom to the surface of the substrate, and σ and ϵ are parameters that relate to the equilibrium distance $r = 0.858\sigma$ and adhesion energy 1.054ϵ per S atom. It is noted that this potential is derived by being integrated over a three-dimensional half-lattice of LJ 12-6 particles, which is suitable to describe the interaction with the Si_3N_4 substrate. In simulations, we use $\sigma = 2.3$ Å, and it gives the equilibrium distance of 2.0 Å, which is the same as the van der Waals radius of the S atom. We test the mechanical strength of the MoS_2 by varying adhesion energy from 0.238 to 7.15 eV/nm^2, which corresponds to $\epsilon = 0.02$ to 0.6 eV in our model, and find that for $\epsilon > 0.24$ eV, increment in ϵ does not affect the strength of the monolayer MoS_2 anymore. We thereafter use $\epsilon = 1.0$ eV through our simulations to ensure the in-plane deformation of the MoS_2 under mechanical loading to study the intrinsic strength and fracture toughness of MoS_2 without some effects from ripples, which agree with what is observed in all of the experiments.

Fracture Tests on Monolayer MoS_2 by Mechanical Force. The time step used for time integration is 0.5 fs in the molecular dynamics simulations. We create a different ratio of defects in the MoS_2 model simply by randomly removing the S atoms by a certain

amount that corresponds to the defect ratio throughout the material at the beginning of the simulation. Before we conduct the mechanical penetration tests, the system is fully equilibrated with increased temperature from 1 to 300 K by using a Langevin thermostat. The molecular dynamics simulation is run in an NVT ensemble (constant number of particles, volume, and temperature) with the temperature controlled by a Nosé-Hoover thermostat. We use a cylindrical nanoindenter model with a stiffness of $K = 0.5$ eV/Å^3 to apply force on the inner layer of the round hole (force on an atom is given by $F(R) = -K(R - R_0(t))^2$, where R is the distance from the central axis of the indenter and $R_0(t)$ is the radius of the indenter at the current time) in the monolayer MoS_2 by increasing the radius of the nanoindenter R_0 in a quasistatic way. For each increment, we linearly increase R_0 from initially 50 Å by $\Delta R_0 = 1$ Å within 10 000 steps, followed by equilibrating the system by both energy minimization and equilibration for 20 000 steps by keeping the R_0 at a constant value. We perform energy minimization and relaxation at every quasistatic step, which allows us to describe the deformation of MoS_2 without the strain rate effect. By repeating the increment process, we are able to deform and fracture the entire MoS_2 model with the cracks propagating from the initial triangular cracks. We compute the total potential energy of the system after full fracture as E_{end} and before mechanical loading as E_{init} and calculate the energy release rate via

$$G_C = (E_{end} - E_{init})/(L - L_0) \tag{2}$$

where $L = 50$ nm is the length of the sample and $L_0 = 14$ nm is the total length of the round hole and two triangular cracks. We find that reducing ΔR_0 does not alter the G_C value. We repeat the penetration test for pristine MoS_2 four times for initial cracks along different material directions (armchair *versus* zigzag) by changing the initial velocity distribution and measuring G_C for each of the simulations. The average values and standard deviations of G_C in armchair *versus* zigzag directions are summarized in Figure 4i for comparison.

ASSOCIATED CONTENT

Ⓢ Supporting Information

The Supporting Information is available free of charge on the ACS Publications website at DOI: 10.1021/acsnano.6b05435.

> Popping the strained MoS_2 monolayer with a focused electron beam; validation of reactive force field for MoS_2 modeling; methods of resolving the lattice structure of MoS_2 around the torn edges; diversity of MoS_2 edge configurations; driving force of crack propagation on MoS_2 under the electron beam; residue chains formed during crack; structure evolution comparison between monolayer MoS_2 and graphene under a continuous electron beam irradiation; Young's modulus, energy release rate, and fracture toughness for defected MoS_2 and graphene; supplementary Tables 1 and 2; and crack propagation in a seriously defective region on monolayer MoS_2 (PDF)
> Video 1 (AVI)
> Video 2 (AVI)

AUTHOR INFORMATION

Corresponding Authors
*E-mail: mbuehler@mit.edu.
*E-mail: jamie.warner@materials.ox.ac.uk.

Author Contributions
§S.W. and Z.Q. contributed equally to this work.

Notes

The authors declare no competing financial interest.

ACKNOWLEDGMENTS

REFERENCES

(1) Buehler, M. J.; Gao, H. Dynamical Fracture Instabilities due to Local Hyperelasticity at Crack Tips. *Nature* **2006**, *439*, 307−310.

(2) Pons, A. J.; Karma, A. Helical Crack-Front Instability in Mixed-Mode Fracture. *Nature* **2010**, *464*, 85−89.

(3) Warner, D. H.; Curtin, W. A.; Qu, S. Rate Dependence of Crack-Tip Processes Predicts Twinning Trends in F.c.c. Metals. *Nat. Mater.* **2007**, *6*, 876−881.

(4) Kermode, J. R.; Albaret, T.; Sherman, D.; Bernstein, N.; Gumbsch, P.; Payne, M. C.; Csányi, G.; De Vita, A. Low-Speed Fracture Instabilities in a Brittle Crystal. *Nature* **2008**, *455*, 1224−1227.

(5) Livne, A.; Bouchbinder, E.; Svetlizky, I.; Fineberg, J. The Near-Tip Fields of Fast Cracks. *Science* **2010**, *327*, 1359−1363.

(6) Hénaux, S.; Creuzet, F. Crack Tip Morphology of Slowly Growing Cracks in Glass. *J. Am. Ceram. Soc.* **2000**, *83*, 415−417.

(7) Buehler, M. J.; Van Duin, A. C. T.; Goddard, W. A. Multiparadigm Modeling of Dynamical Crack Propagation in Silicon Using a Reactive Force Field. *Phys. Rev. Lett.* **2006**, *96*, 095505.

(8) Nam, K. H.; Park, I. H.; Ko, S. H. Patterning by Controlled Cracking. *Nature* **2012**, *485*, 221−224.

(9) Wang, D.; Zhao, J.; Hu, S.; Yin, X.; Liang, S.; Liu, Y.; Deng, S. Where, and How, Does a Nanowire Break? *Nano Lett.* **2007**, *7*, 1208−1212.

(10) Cleri, F.; Yip, S.; Wolf, D.; Phillpot, S. Atomic-Scale Mechanism of Crack-Tip Plasticity: Dislocation Nucleation and Crack-Tip Shielding. *Phys. Rev. Lett.* **1997**, *79*, 1309−1312.

(11) Bitzek, E.; Kermode, J. R.; Gumbsch, P. Atomistic Aspects of Fractures. *Int. J. Fract.* **2015**, *191*, 13−30.

(12) Liu, L.; Wang, J.; Gong, S. K.; Mao, S. X. Atomistic Observation of a Crack Tip Approaching Coherent Twin Boundaries. *Sci. Rep.* **2014**, *4*, 4397.

(13) Zhao, C. W.; Xing, Y. M. Nanoscale Experimental Study of a Micro-Crack in Silicon. *Phys. B* **2008**, *403*, 4202−4204.

(14) Goswami, R.; Pande, C. S. Investigations of Crack-Dislocation Interactions ahead of Mode-III Crack. *Mater. Sci. Eng., A* **2015**, *627*, 217−222.

(15) Litorowicz, A. Identification and Quantification of Cracks in Concrete by Optical Fluorescent Microscopy. *Cem. Concr. Res.* **2006**, *36*, 1508−1515.

(16) Guilloteau, E.; Charrue, H.; Creuzet, F. The Direct Observation of the Core Region of a Propagating Fracture Crack in Glass. *Europhys. Lett.* **1996**, *34*, 549−554.

(17) Marques, M. A. L.; Troiani, H. E.; Miki-Yoshida, M.; Jose-Yacaman, M.; Rubio, A. On the Breaking of Carbon Nanotubes under Tension. *Nano Lett.* **2004**, *4*, 811−815.

(18) Barreiro, A.; Börrnert, F.; Rümmeli, M. H.; Büchner, B.; Vandersypen, L. M. K. Graphene at High Bias: Cracking, Layer by Layer Sublimation, and Fusing. *Nano Lett.* **2012**, *12*, 1873−1878.

(19) Zhou, W.; Zou, X.; Najmaei, S.; Liu, Z.; Shi, Y.; Kong, J.; Lou, J.; Ajayan, P. M.; Yakobson, B. I.; Idrobo, J.-C. Intrinsic Structural Defects in Monolayer Molybdenum Disulfide. *Nano Lett.* **2013**, *13*, 2615−2622.

(20) Alem, N.; Erni, R.; Kisielowski, C.; Rossell, M. D.; Gannett, W.; Zettl, A. Atomically Thin Hexagonal Boron Nitride Probed by Ultrahigh-Resolution Transmission Electron Microscopy. *Phys. Rev. B: Condens. Matter Mater. Phys.* **2009**, *80*, 155425.

(21) Zhang, Z.; Kutana, A.; Yakobson, B. I. Edge Reconstruction-Mediated Graphene Fracture. *Nanoscale* **2015**, *7*, 2716−2722.

(22) Terdalkar, S. S.; Huang, S.; Yuan, H.; Rencis, J. J.; Zhu, T.; Zhang, S. Nanoscale Fracture in Graphene. *Chem. Phys. Lett.* **2010**, *494*, 218−222.

(23) Jung, G.; Qin, Z.; Buehler, M. J. Molecular Mechanics of Polycrystalline Graphene with Enhanced Fracture Toughness. *Extrem. Mech. Lett.* **2015**, *2*, 52−59.

(24) López-Polín, G.; Gómez-Herrero, J.; Gómez-Navarro, C. Confining Crack Propagation in Defective Graphene. *Nano Lett.* **2015**, *15*, 2050−2054.

(25) Kim, K.; Artyukhov, V. I.; Regan, W.; Liu, Y.; Crommie, M. F.; Yakobson, B. I.; Zettl, A. Ripping Graphene: Preferred Directions. *Nano Lett.* **2012**, *12*, 293−297.

(26) Jack, R.; Sen, D.; Buehler, M. J. Graphene Nanocutting through Nanopatterned Vacancy Defects. *J. Comput. Theor. Nanosci.* **2010**, *7*, 354−359.

(27) Yazyev, O. V.; Louie, S. G. Topological Defects in Graphene: Dislocations and Grain Boundaries. *Phys. Rev. B: Condens. Matter Mater. Phys.* **2010**, *81*, 195420.

(28) Zhang, P.; Ma, L.; Fan, F.; Zeng, Z.; Peng, C.; Loya, P. E.; Liu, Z.; Gong, Y.; Zhang, J.; Zhang, X.; Ajayan, P. M.; Zhu, T.; Lou, J. Fracture Toughness of Graphene. *Nat. Commun.* **2014**, *5*, 3782.

(29) Wang, S.; Rong, Y.; Fan, Y.; Pacios, M.; Bhaskaran, H.; He, K.; Warner, J. H. Shape Evolution of Monolayer MoS_2 Crystals Grown by Chemical Vapor Deposition. *Chem. Mater.* **2014**, *26*, 6371−6379.

(30) Wang, S.; Wang, X.; Warner, J. H. All Chemical Vapor Deposition Growth of MoS_2:h-BN Vertical van der Waals Heterostructures. *ACS Nano* **2015**, *9*, 5246−5254.

(31) Kim, K.; Coh, S.; Kisielowski, C.; Crommie, M. F.; Louie, S. G.; Cohen, M. L.; Zettl, A. Atomically Perfect Torn Graphene Edges and Their Reversible Reconstruction. *Nat. Commun.* **2013**, *4*, 2723.

(32) Stewart, J. A.; Spearot, D. E. Atomistic Simulations of Nanoindentation on the Basal Plane of Crystalline Molybdenum Disulfide (MoS). *Modell. Simul. Mater. Sci. Eng.* **2013**, *21*, 045003.

(33) Liang, T.; Phillpot, S. R.; Sinnott, S. B. Parametrization of a Reactive Many-Body Potential for Mo−S Systems. *Phys. Rev. B: Condens. Matter Mater. Phys.* **2009**, *79*, 245110.

(34) Giannozzi, P.; Baroni, S.; Bonini, N.; Calandra, M.; Car, R.; Cavazzoni, C.; Ceresoli, D.; Chiarotti, G. L.; Cococcioni, M.; Dabo, I.; Dal Corso, A.; de Gironcoli, S.; Fabris, S.; Fratesi, G.; Gebauer, R.; Gerstmann, U.; Gougoussis, C.; Kokalj, A.; Lazzeri, M.; Martin-Samos, L.; et al. QUANTUM ESPRESSO: A Modular and Open-Source Software Project for Quantum Simulations of Materials. *J. Phys.: Condens. Matter* **2009**, *21*, 395502.

(35) Perdew, J. P.; Burke, K.; Ernzerhof, M. Generalized Gradient Approximation Made Simple. *Phys. Rev. Lett.* **1996**, *77*, 3865−3868.

(36) Troullier, N.; Martins, J. L. Efficient Pseudopotentials for Plane-Wave Calculations. *Phys. Rev. B: Condens. Matter Mater. Phys.* **1991**, *43*, 1993−2006.

(37) Cooper, R. C.; Lee, C.; Marianetti, C. A.; Wei, X.; Hone, J.; Kysar, J. W. Nonlinear Elastic Behavior of Two-Dimensional Molybdenum Disulfide. *Phys. Rev. B: Condens. Matter Mater. Phys.* **2013**, *87*, 035423.

(38) Xiong, S.; Cao, G. Molecular Dynamics Simulations of Mechanical Properties of Monolayer MoS_2. *Nanotechnology* **2015**, *26*, 185705.

(39) Li, T. Ideal Strength and Phonon Instability in Single-Layer MoS_2. *Phys. Rev. B: Condens. Matter Mater. Phys.* **2012**, *85*, 235407.

(40) Shenderova, O. A.; Brenner, D. W.; Omeltchenko, A.; Su, X.; Yang, L. H. Atomistic Modeling of the Fracture of Polycrystalline Diamond. *Phys. Rev. B: Condens. Matter Mater. Phys.* **2000**, *61*, 3877−3888.

(41) Wei, Y.; Wu, J.; Yin, H.; Shi, X.; Yang, R.; Dresselhaus, M. The Nature of Strength Enhancement and Weakening by Pentagon−heptagon Defects in Graphene. *Nat. Mater.* **2012**, *11*, 759−763.

(42) Magda, J. J.; Tirrell, M.; Davis, H. T. Molecular Dynamics of Narrow, Liquid-Filled Pores. *J. Chem. Phys.* **1985**, *83*, 1888−1901.